PAPER • **OPEN ACCESS**

Flower-like N-doped MoS_2 for photocatalytic degradation of RhB by visible light irradiation

To cite this article: Peitao Liu *et al* 2016 *Nanotechnology* **27** 225403

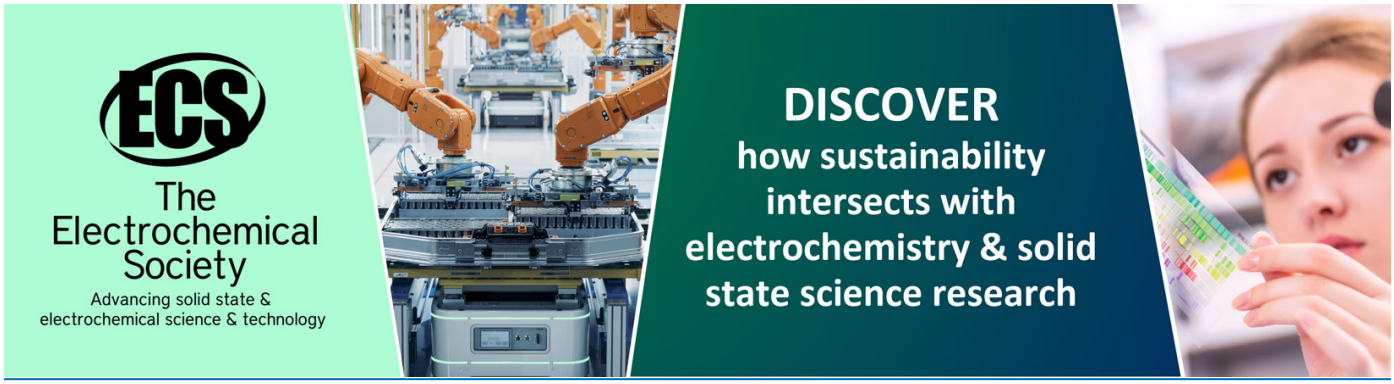

OPEN ACCESS
IOP Publishing
Nanotechnology

Nanotechnology **27** (2016) 225403 (8pp)
doi:10.1088/0957-4484/27/22/225403

Flower-like N-doped MoS_2 for photocatalytic degradation of RhB by visible light irradiation

Peitao Liu[1], Yonggang Liu[1], Weichun Ye[2], Ji Ma and Daqiang Gao[1]

[1] Key laboratory for magnetism and Magnetic Materials of MOE, Lanzhou University, Lanzhou 730000, People's Republic of China
[2] Department of Chemistry, Lanzhou University, Lanzhou 730000, People's Republic of China

E-mail: yewch@lzu.edu.cn and gaodq@lzu.edu.cn

Received 19 January 2016, revised 24 March 2016
Accepted for publication 31 March 2016
Published 25 April 2016

Abstract

In this paper, the photocatalytic performance and reusability of N-doped MoS_2 nanoflowers with the specific surface area of 114.2 m^2 g^{-1} was evaluated by discoloring of RhB under visible light irradiation. Results indicated that the 20 mg fabricated catalyst could completely degrade 50 ml of 30 mg l^{-1} RhB in 70 min with excellent recycling and structural stability. The optimized N-doped MoS_2 nanoflowers showed a reaction rate constant (k) as high as 0.06928 min^{-1} which was 26.4 times that of bare MoS_2 nanosheets ($k = 0.00262$). In addition, it was about seven times that of P25 ($k = 0.01$) (Hou *et al* 2015 *Sci. Rep.* **5** 15228). The obtained outstanding photocatalytic performance of N-doped MoS_2 nanoflowers provides potential applications in water pollution treatment, as well as other related fields.

S Online supplementary data available from stacks.iop.org/NANO/27/225403/mmedia

Keywords: photocatalysis, electron–hole pairs, hydroxyl radical, N-doped MoS_2 nanoflowers

(Some figures may appear in colour only in the online journal)

1. Introduction

Persistent organic pollutants in underground water have already become serious problems that influence the survival the environment of human beings and other creatures. Effluents from the textile industries are important sources of water pollution, because dyes in wastewater undergo chemical as well as biological changes, consume dissolved oxygen, destroy aquatic life and endanger human health. It is necessary to disintegrate textile effluents into the receiving-water standard [2–7]. Hence, in recent years, numerous investigations have been devoted to developing products to address the challenges of water pollution, such as TiO_2 [8], ZnO [9], N-TiO_2@g-C_3N_4 [10], N-doped ZnO@g-C_3N_4 [11], TiO_2 hollow fibers [1], etc.

As a representative two-dimensional (2D) layered transition metal sulfide [12–16], molybdenum disulfide (MoS_2) nanosheets possess many superior photoelectric characteristics, such as excellent electrocatalytic performance [17], higher absorbance in the near-infrared region [18], high chemical stability [19], strong absorption in the visible frequencies [20], large carrier mobility [21], and direct bandgap [22]. These excellent characteristics of MoS_2 drive photocatalytic researchers to combine it with other semiconductors, such as MoS_2@$BiVO_4$ hetero-nanoflowers [23], MoS_2@g-C_3N_4 heterostructures (5 mg sample, 50 ml 5 mg l^{-1} RhB, 20 min) [24], nano-MoS_2@TiO_2 composites [25], and MoS_2@CdS branch-like heterostructures (30 mg sample, 50 ml 10 mg l^{-1} RhB, 50 min) [26]. These composites have been reported to be used to degrade organic pollution owing to their highly photocatalytic efficiency, offering potential applications in future industrial decontamination. However,

complicated processes and/or poisonous components during synthesis make them insufficient [27, 28].

An alternative is to search for novel highly efficient photocatalysts with simple phase structure and synthesis process. In this paper, we report the excellent photocatalytic activities of N-doped MoS_2 nanoflowers in degrading the organic dye of RhB, synthesized by a simple sol–gel method. The fabricated N-doped MoS_2 nanoflowers have a high surface area of 114.2 $m^2\,g^{-1}$, and possess a high adsorption property of small concentrations of RhB (see supplementary data S1 (stacks.iop.org/NANO/27/225403/mmedia)), as well as excellent photocatalytic activity in degrading 30 $mg\,l^{-1}$ RhB. The outstanding photocatalytic activities of as-prepared flower-like N-doped MoS_2 samples could also be extended to degrade other organic dyes and heavy metal pollutants, providing potential applications in future water pollution treatment.

2. Experiment

N-doped MoS_2 nanoflowers were synthesized by an optimized sol–gel method as previously reported [29]. In brief, 2 g thiourea was mixed with 0.5 g $MoCl_5$ by dropwise addition of alcohol. Then the brown gel-like precursor powders were formed after drying. Next, the precursor powders were transferred into a quartz boat and heated in a tube furnace for 2 h under 0.1 L min^{-1} argon flow at 550 °C. To get its bulk form, we changed the annealing temperature to 1050 °C.

To compare, pure MoS_2 nanosheets were prepared by the hydrothermal method, where 1 mmol ammonium molybdate tetrahydrate and 30 mmol thiourea were dissolved in 40 ml deionized water under magnetic stirring. Then, the solution was transferred to a 50 ml reaction still and maintained at 200 °C for 20 h before being cooled down in air.

α-Fe_2O_3@N-doped MoS_2 heterostructures were synthesized by the hydrothermal method, where 90 mg N-doped MoS_2 was dissolved in 32 ml deionized water. Then, 0.202 g $Fe(NO_3)_3 \cdot 9H_2O$ and 0.3 g $CO(NH_2)_2$ were dissolved in the above solution under magnetic stirring. After that, 0.006 g sodium dodecyl benzenesulphonate (SDBS) was added into the above solution and continuously stirred in a water bath of 60 °C for 30 min. Finally, the solution was transferred to a 40 ml reactor and maintained at 90 °C for 12 h before being cooled down in air.

The crystal structure of the samples was measured by x-ray diffractometry (XRD) in a Philips/X, Pert PRO diffractometer with Cu *Ka* radiation. A scanning electron microscope (SEM, Hitachi S-4800) and high resolution transmission electron microscope (HRTEM, TecnaiTM G2 F30, FEI, USA) were used to observe the morphology and structure of the samples. In addition, x-ray photoelectron spectroscopy (XPS, VG Scientific ESCALAB-210) was employed to study the chemical nature of N, Mo, and S with Al *Ka* x-ray. The Brunauer–Emmett–Teller (BET) surface area and pore width were measured using a Micrometrics ASAP 2020 V403. Meanwhile, Raman spectra were measured at room temperature using a Jobin-Yvon HR 800 spectrometer.

The photocatalytic activity of the samples was measured by degradation of RhB with a 175 W halogen lamp. 50 ml RhB (30 $mg\,l^{-1}$) was placed in a glass. Meanwhile, 20 mg photocatalyst was added under constant stirring. Photocalytic activity of the samples was evaluated under visible light irradiation. At certain time intervals, 4 ml solution was taken out, where the photocatalyst was removed by a centrifugal machine. Then, the filtrates were analyzed by recording variations of the absorption band maximum (553 nm) in the UV–vis spectra of RhB. In addition, the recyclability of the samples was also investigated.

3. Results and discussion

3.1. Characterization

As shown in figure 1(a), the obtained products and the used sample (N-doped MoS_2 nanoflowers were used for photocatalytic activity testing) were measured by XRD. Results indicate that all the diffraction peaks can be indexed as hexagonal MoS_2. For the used sample, the characteristic peaks were similar to primitive products, indicating our sample has a stable structure in the photocatalytic process, which is also confirmed by the further Raman study as illustrated in figure 1(b). As can be seen, the two distinct peaks located around 378 cm^{-1} and 402 cm^{-1} correspond to the MoS_2 characteristic signature, associated with in-plane E^1_{2g} (the in-plane displacement of Mo and S atoms) and out-of-plane A_{1g} (out-of-plane symmetric displacements of S atoms along the *c*-axis) Raman mode, respectively [12, 30]. SEM and TEM measurements were employed to study the morphology of the products. As shown in figure 1(c), the fabricated sample has a flower-like structure and each of the components shows nanosheet features. As illustrated in figures 1(d) and (e), the TEM images also show the nanoflower-structure of the product, which is consist with the SEM results. Meanwhile, the results also reveal the typical structure of the nanosheets, containing 3–5 layers from the curly edges. Energy-dispersive x-ray spectroscopy (EDS) mapping was carried out to verify the element distribution. It clearly shows the presence of elements Mo, S, and N in the product, and the N element was evenly distributed in the sample.

The XPS spectrum was employed to examine the surface electronic state and composition of the flower-like N-doped MoS_2. The whole XPS spectrum further indicates the sample contains N, S, and Mo elements, as shown in figure 2(a), in agreement with the EDS mapping results. In addition, figure 2(b) shows a high-resolution spectrum in the binding energy range of 390–405 eV. Generally, the peak at 396.2 eV corresponds to Mo $3p_{3/2}$ and there is a hump on the side of the Mo $3p_{3/2}$ peak which originates from the N-Mo bond [29]. The crossover peak at 399.2 eV corresponds to N 1S peak from the Mo-N bond [31, 32]. Besides, another peak at 402.1 eV is considered to be the N 1s peak attributed to the NO absorbed on the surface of the MoS_2 [33]. These results

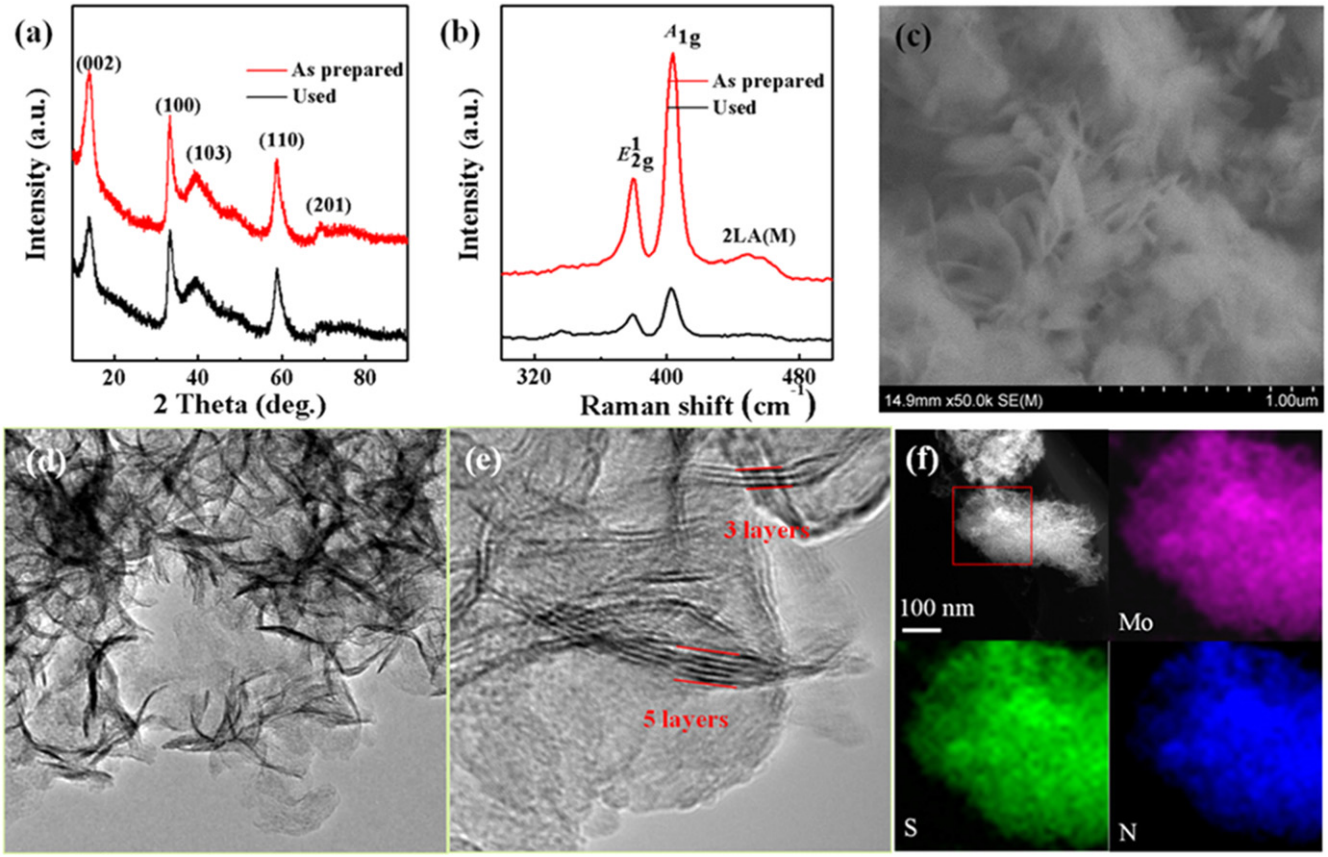

Figure 1. (a) XRD patterns and (b) Raman spectra of fresh fabricated and used sample of N-doped MoS_2 nanoflowers. (c) SEM, (d) TEM, (e) HRTEM image, and (f) EDS mapping of N-doped MoS_2 nanoflowers.

indicate the S sites were replaced by N on MoS_2. In addition, BET nitrogen adsorption analysis was performed to further study the specific surface area of the sample. As shown in figure 2(c), when the relative pressure $P/P_0 > 0.05$, the amount of absorbed nitrogen increases rapidly with the increase of the relative pressure, indicating the process of adsorption of multi-layers [34]. Results indicate that the BET surface of the N-doping MoS_2 nanoflowers is 114.2 m^2 g^{-1} and the size of the pore width ranges from 1.7 nm to 30 nm, as shown in figure 2(d). These results indicate the fabricated sample has a large surface area and pore size distribution.

To investigate the optical properties of the fabricated N-doped MoS_2 nanoflowers, UV–vis spectra were considered and the results are presented in figure 3(a) (the result of the MoS2 nanosheets is also presented to compare). It can be seen from figure 3(a) that the samples exhibit an enhanced strong light absorption in the wavelength range of 200–800 nm. As shown in figure 3(b), the band gap of the samples is estimated from the plot of $(ahv)^n$ versus hv by extrapolating the straight line to the X axis intercept. Results indicate that N-doped MoS_2 nanoflowers (2.08 eV) have a narrow band gap in comparison with MoS_2 nanosheets (2.17 eV). The UV–vis diffuse reflectance spectra (DRS) results indicate that more photogenerated charges are generated when flower-like N-doped MoS_2 is excited under visible light irradiation, which enhances the photocatalytic performance [35, 36].

3.2. Photocatalytic activity

Photocatalytic performances of the N-doped MoS_2 nanoflowers were evaluated by degrading RhB aqueous solution at room temperature under visible light irradiation. As shown in figure 4(a), the concentration of the RhB decreases as the test time increases for all the photocatalysts. As can be clearly seen, the degrading rate of RhB with the photocatalysts follows the order of: N-doped MoS_2 nanoflower > without light (flower-like N-doping MoS_2 heterostructure in a dark condition) > MoS_2 nanosheets > bulk N-doped MoS_2. This result indicates that the prepared N-doped MoS_2 nanoflowers have better photocatalytic properties than others. Meanwhile, in the dark condition, the degradation efficiency of RhB for the N-doped MoS_2 nanoflowers is only 12%, indicating that light plays a key role in degradation of RhB. Plots of the absorbance versus wavelength for degradation of RhB for N-doped MoS_2 nanoflowers at various irradiation times are shown in figure 4(b). It can be seen that the intensity of the absorption peaks continuously decreases without any change in position during the degradation reactions. To further examine the role of the surface area in photocatalytic reactions, plots of $\ln(C/C_0)$ versus irradiation time are displayed in figure 4(c) (the initial concentration of the RhB suspension was measured and used as the initial concentration C_0; in addition, C is the actual concentration of RhB at the indicated reaction time). It can be seen that both the curves are linear,

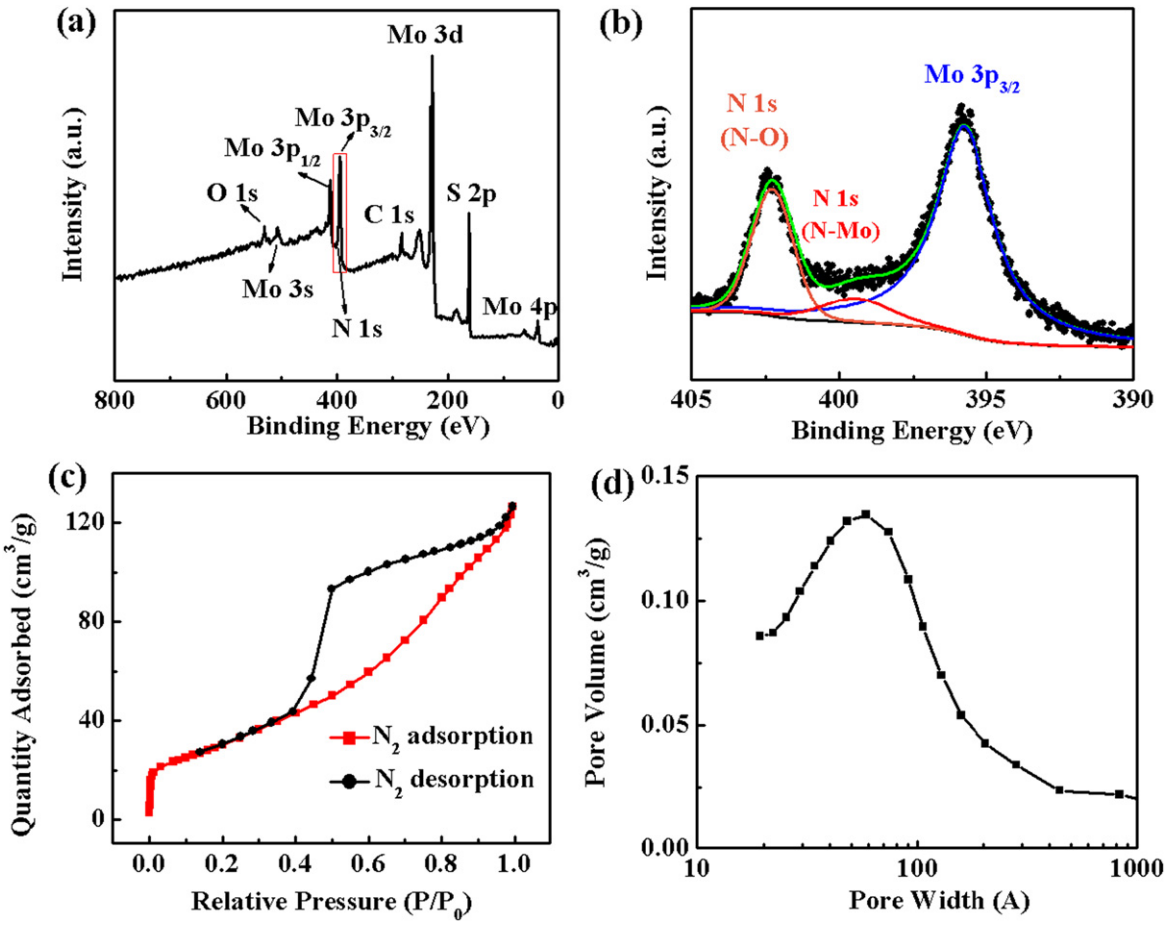

Figure 2. (a) XPS spectrum, (b) high-resolution XPS spectrum, (c) nitrogen adsorption–desorption isotherm curve, and (d) pore size distribution curve of N-doped MoS_2 nanoflowers.

indicating photodegradation of the RhB goes through a pseudo-first-order kinetic reaction [35]. Besides, the potocatalytic activity of N-doped MoS_2 nanoflowers under visible light irradiation is higher than that of MoS_2 nanosheets because N-doped MoS_2 nanoflowers have a large surface area and large pore size distribution (see supplementary data S2 (stacks.iop.org/NANO/27/225403/mmedia)) [37]. N doping could also extend the spectral response to visible light and greatly improve the utilization of visible light [38, 39]. The stability of photocatalysts is a crucial factor for their assessment and practical applications. Figure 4(d) shows the recycling reaction towards degradation of RhB with the catalyst of N-doped MoS_2 nanoflowers, where the sample was separated by a centrifuge after every 70 min of visible light irradiation. Results indicate the photocatalytic performance of the N-doped MoS_2 nanoflowers do not decrease obviously after four consecutive experiments, revealing its excellent recycling and structural stability.

3.3. Discussion of the photocatalytic mechanism of N-doped MoS_2 nanoflowers

In order to give further evidence to support the photocatalytic mechanism, the transient photocurrent responses of an N-doped MoS_2 nanoflowers electrode were recorded for several on-off cycles of irradiation. Figure 5(a) shows the photocurrent-time testing curves of the N-doped MoS_2 nanoflowers. Results indicate our photocatalyst has the highest photocurrent compared to graphene/C_3N_4 composites [40], g-C_3N_4/Zn_2GeO_4 heterojunctions [41], g-C_3N_4/NiS hybrid [42], and grapheme oxide/graphitic-C_3N_4 nanosheet hybrid [43]. Generally, the value of the photocurrent indirectly reflects the ability to generate and transfer the photoexcited charge carrier under irradiation [44]. The higher the photocurrent is, the higher the e^+-h^+ separation efficiency [40, 45]. To further study the photocatalytic mechanism of the sample, radical trapping experiments were proposed. In radical trapping experiments, ammonium oxalate (AO, 5 ml), 1, 4-benzoquinone (BQ, 5 ml) and tertiary butyl alcohol (TBA, 5 ml) were used as scavengers of the photo-induced holes (h^+), superoxide radicals ($\cdot O_2^-$), and hydroxyl radicals ($\cdot$OH), respectively [35, 46–48]. Displayed in figure 5(b) is the degradation efficiency of RhB from 100% to 5% in the presence of TBA compared to that with no radical scavengers under visible light irradiation. Meanwhile, the degradation efficiencies of RhB reach 15% and 40% in the presence of AO and BQ, respectively. Thus, it is reasonable to conclude that h^+, $\cdot O_2^-$, and $\cdot$OH as oxidation species were indeed photogenerated on catalyst surfaces and are responsible for the photocatalytic degradation. In general, the more positive

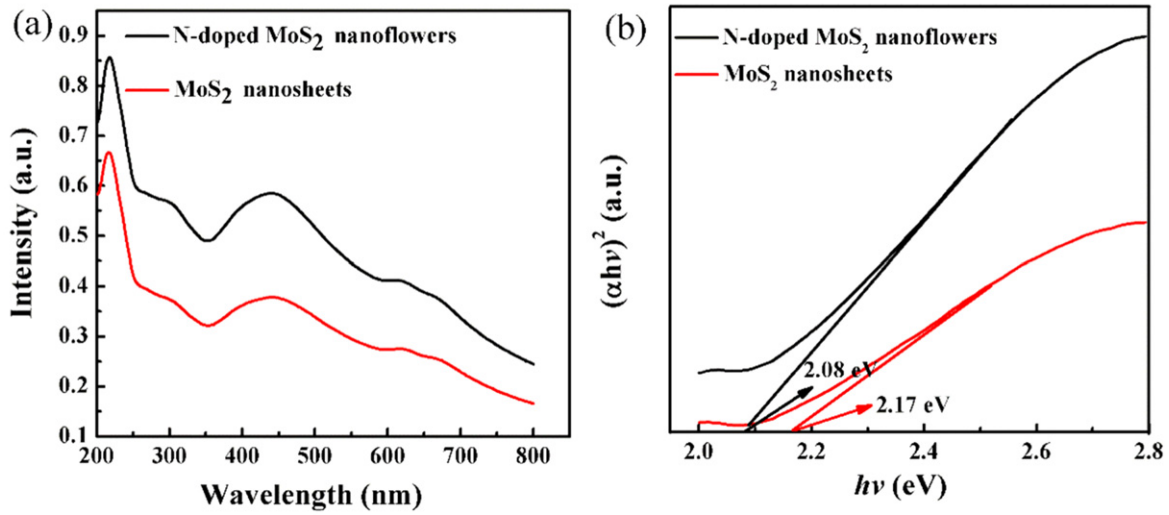

Figure 3. (a) UV–vis DRS and (b) estimated band-gap energy of N-doped MoS_2 nanoflowers and MoS_2 nanosheets.

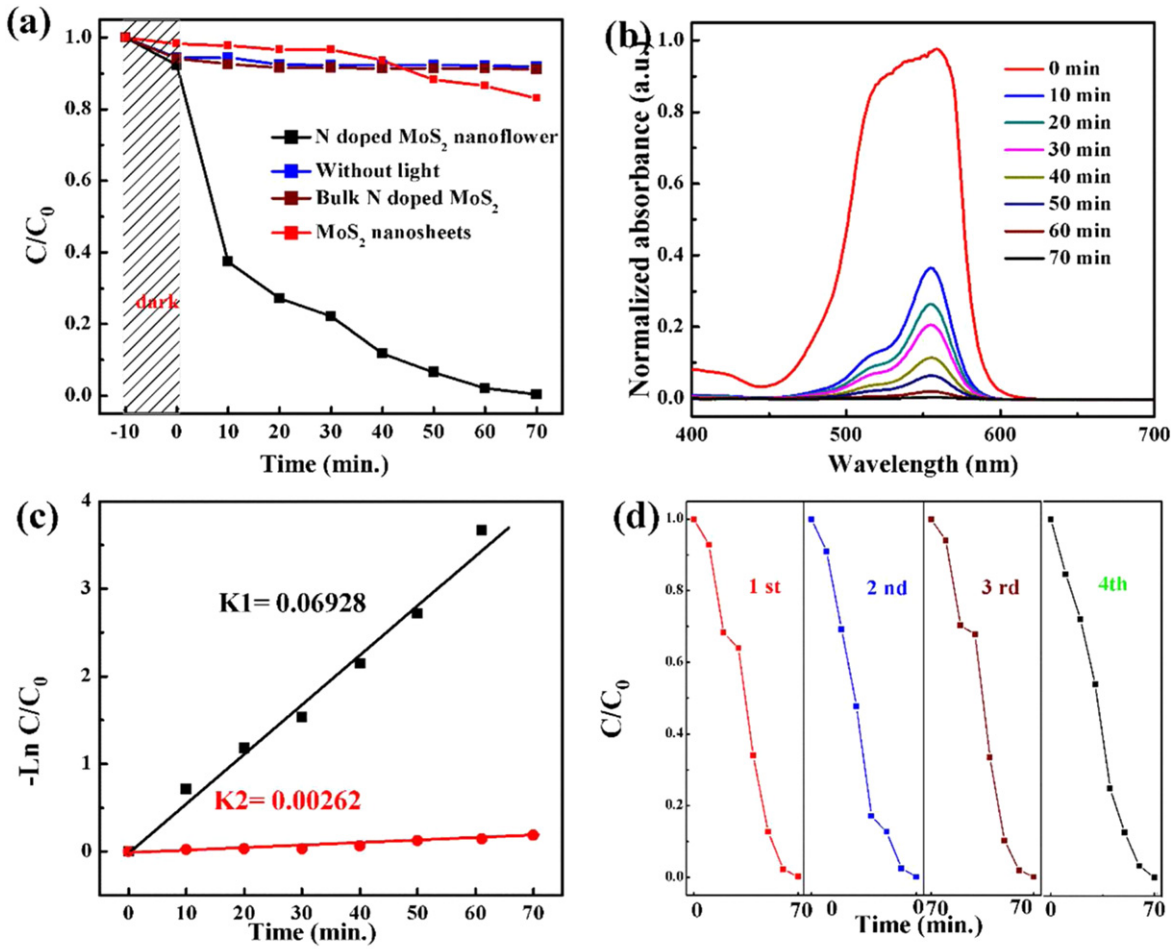

Figure 4. (a) Photocatalytic degradation of RhB by different photocatalysts under visible light irradiation. (b) UV–vis spectroscopic changes of the RhB aqueous solution in the presence of N-doped MoS_2 nanoflowers. (c) Plot of $\ln(C_0/C)$ with irradiation time for N-doped MoS_2 nanoflowers and MoS_2 nanosheets. (d) Reusability experiment for degradation of RhB by N-doped MoS_2 nanoflowers under visible light irradiation.

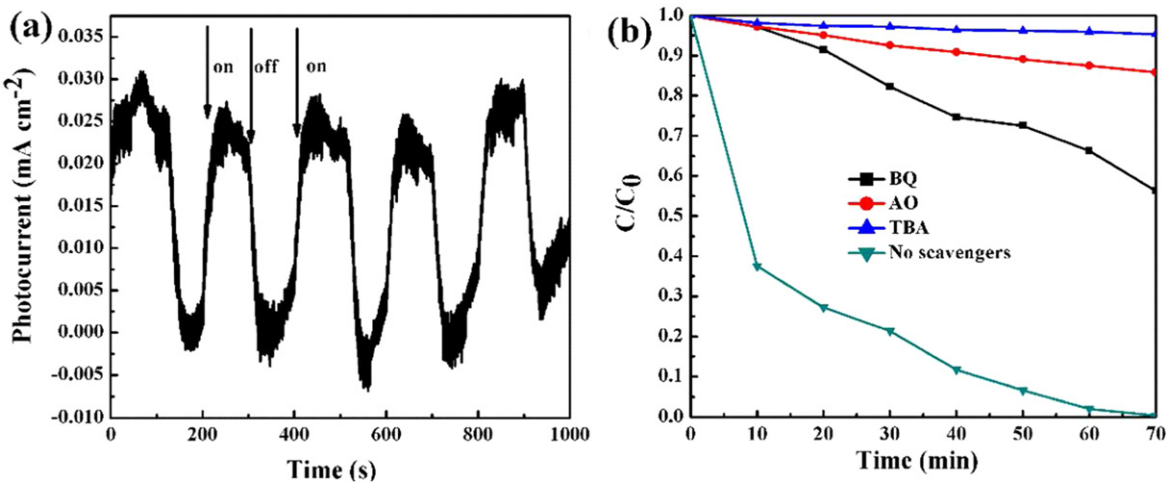

Figure 5. (a) Transient photocurrent responses and (b) radical trapping experiments of flower-like N-doped MoS_2 nanoflowers.

the valence band potential, the stronger the oxidation ability of photogenerated holes, which is favored for better photocatalytic activity [49]. So it can be concluded that direct oxidation by holes is crucial because the potential of photogenerated holes is so positive that it can effectively oxidize dyes directly. In addition, hydroxyl radicals are more important than other radicals for dye degradation due to transformation of the parts of $\cdot O_2^-$ into ·OH radicals.

Based on above results, N-doped MoS_2 nanoflowers with excellent photocatalytic performance might be explained by the following factors. First of all, N-doped MoS_2 nanoflowers have larger BET areas (figures 2(c) and (d)), which can not only improve surface adsorption capacity of the reactants, but also expose more active sites, guaranteeing higher activity in degrading RhB [50, 51]. In addition, as shown in figure 3, N-doped MoS_2 nanoflowers have a narrow band gap compared with MoS_2 nanosheets, which can extend the spectral response to visible light and greatly improve the utilization of visible light [38, 39], guaranteeing higher activity in degrading RhB. Moreover, N doping extends the visible light absorption edge and electrons sre excited from the N impurity level to the conduction band, guaranteeing higher activity in degrading RhB [52]. Meanwhile, electrons in the CB of N-doped MoS_2 flowers are good reductants that could efficiently change the O_2 absorbed onto the catalyst surface into various reactive species ($O_2\cdot^-$, HO_2, H_2O_2), subsequently leading to the formation of ·OH and oxidation of RhB into CO_2, H_2O, etc. Based on the above results and discussion, we propose a possible mechanism (figure 6) to explain the degradation of RhB by N-doped MoS_2 nanoflowers under visible light irradiation. The radical production could be expressed by reactions as follows:

$$\text{N-doped } MoS_2 + h\nu \rightarrow \text{N-doped } MoS_2\,(h^+/e^-) \quad (1)$$

$$O_2 + e^- \rightarrow \cdot O_2^- \quad (2)$$

$$H_2O + h^+ \rightarrow \cdot OH + H^+ \quad (3)$$

$$\cdot O_2^- + 2H^+ + e^- \rightarrow H_2O_2 \quad (4)$$

$$H_2O_2 + e^- \rightarrow \cdot OH + OH^- \quad (5)$$

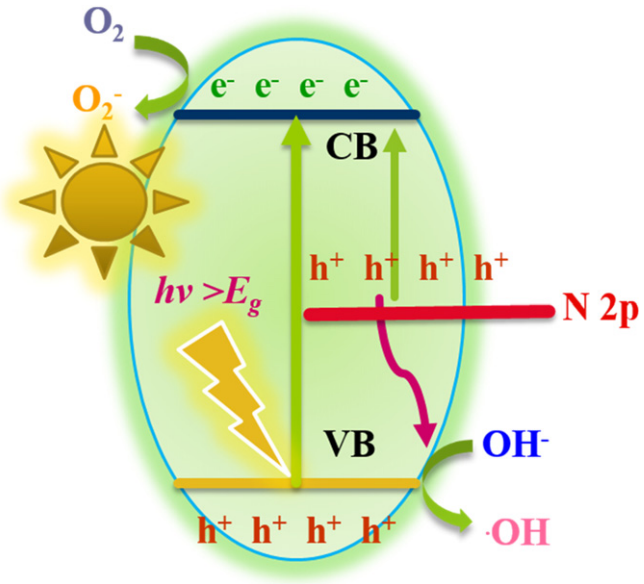

Figure 6. Illustration of RhB degradation by N-doped MoS_2 nanoflowers.

$$h^+ + OH^- \rightarrow \cdot OH \quad (6)$$

$$\cdot OH,\ \cdot O_2^-,\ h^+ + RhB \rightarrow CO_2 + H_2O \quad (7)$$

Although as-prepared N-doped MoS_2 nanoflowers show obvious photocatalysis, it is not so easy to recycle. Recently, magnetically separable semiconductor materials have attracted increasing attention because of their efficient recycling in water treatment and organic dye pollution. Hence, numerous investigations have been devoted to developing magnetic semiconductor materials such as $ZnFe_2O_4@C_3N_4$ [35], $Fe_3O_4@TiO_2$ [53], $BiOCl@SrFe_{12}O_{19}$ [54], etc. Here, α-Fe_2O_3@N-doped MoS_2 nanoflower heterostructures with strong magnetic properties were employed to magnetically separate our catalysts from the solution of RhB. As shown in figure 7, the degradation rate of RhB is almost the same for the catalysts of α-Fe_2O_3@N-doped MoS_2 heterostructures

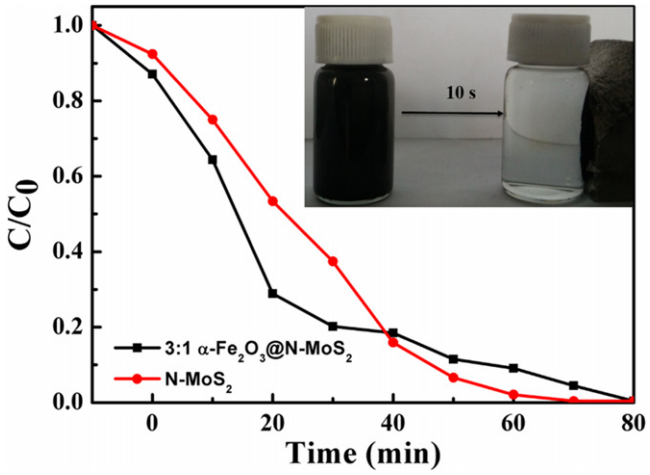

Figure 7. Photocatalytic degradation of RhB by N-doped MoS_2 nanoflowers and α-Fe_2O_3@N-doped MoS_2 heterostructure under visible light irradiation.

and N-doped MoS_2 nanoflowers, but with magnetic separation in 10 s (shown in the upper right of figure 7). These results indicate that α-Fe_2O_3@N-doped MoS_2 heterostructure can not only serve as highly efficient photocatalysts, but also easily separate organic pollutants.

4. Conclusion

In summary, we investigated RhB removal with N-doped MoS_2 nanoflowers and α-Fe_2O_3@N-doped MoS_2 heterostructures. Results indicated that the as-prepared N-doped MoS_2 nanoflowers showed excellent photocatalytic activities and durability on the elimination of the organic pollutants under visible light irradiation. We also demonstrated that the α-Fe_2O_3@N-doped MoS_2 heterostructures can be easily separated from organic pollutants for recycling owing to their magnetic properties. This work helps us to deeply understand the uncommon photophysical processes necessary for the design of highly efficient photocatalysts for environmental applications in the future.

Acknowledgments

This work is supported by the National Basic Research Program of China (Grant No. 2012CB933101), the National Natural Science Fundation of China (Grant No. 51202101, 11474137 and 51301081), and the Fundamental Research Funds for the Central Universities (no. lzujbky-2015-111).

References

[1] Hou H, Shang M, Wang L, Li W, Tang B and Yang W 2015 Efficient photocatalytic activities of TiO_2 hollow fibers with mixed phases and mesoporous walls *Sci. Rep.* **5** 15228
[2] Zhao M, Tang Z and Liu P 2008 Removal of methylene blue from aqueous solution with silica nano-sheets derived from vermiculite *J. Hazard. Mater.* **158** 43–51
[3] Zhao M and Liu P 2008 Adsorption behavior of methylene blue on halloysite nanotubes *Microporous Mesoporous Mater.* **112** 419–24
[4] Yang D J, Zheng Z F, Zhu H Y, Liu H W and Gao X P 2008 Titanate nanofibers as intelligent absorbents for the removal of radioactive ions from water *Adv. Mater.* **20** 2777–81
[5] Legrini O, Oliveros E and Braun A M 1993 Photochemical processes for water treatment *Chem. Rev.* **93** 671–98
[6] Kaur A and Gupta U 2009 A review on applications of nanoparticles for the preconcentration of environmental pollutants *J. Mater. Chem.* **19** 8279
[7] Baiju K V, Shukla S, Biju S, Reddy M L P and Warrier K G K 2009 Hydrothermal processing of dye-adsorbing one-dimensional hydrogen titanate *Mater. Lett.* **63** 923–6
[8] Ihara T, Miyoshi M, Ando M, Sugihara S and Iriyama Y 2001 Preparation of a visible-light-active TiO_2 photocatalyst by RF plasma treatment *J. Mater. Sci.* **36** 4201–7
[9] Tian C, Zhang Q, Wu A, Jiang M, Liang Z, Jiang B and Fu H 2012 Cost-effective large-scale synthesis of ZnO photocatalyst with excellent performance for dye photodegradation *Chem. Commun.* **48** 2858–60
[10] Wang X-J, Yang W-Y, Li F-T, Xue Y-B, Liu R-H and Hao Y-J 2013 *In situ* microwave-assisted synthesis of porous N-TiO2/g-C3N4Heterojunctions with enhanced visible-light photocatalytic properties *Ind. Eng. Chem. Res.* **52** 17140–50
[11] Kumar S, Baruah A, Tonda S, Kumar B, Shanker V and Sreedhar B 2014 Cost-effective and eco-friendly synthesis of novel and stable N-doped ZnO/g-C_3N_4 core–shell nanoplates with excellent visible-light responsive photocatalysis *Nanoscale* **6** 4830–42
[12] Zhou J, Qin J, Zhang X, Shi C, Liu E, Li J, Zhao N and He C 2015 2D space-confined synthesis of few-layer MoS_2 anchored on carbon nanosheet for lithium-ion battery anode *ACS Nano* **9** 3837–48
[13] Huang X, Zeng Z Y and Zhang H 2013 Metal dichalcogenide nanosheets: preparation, properties and applications *Chem. Soc. Rev.* **42** 1934–46
[14] Tan C L and Zhang H 2015 Two-dimensional transition metal dichalcogenide nanosheet-based composites *Chem. Soc. Rev.* **44** 2713–31
[15] Hu Z, Wang L X, Zhang K, Wang J B, Cheng F Y, Tao Z L and Chen J 2014 MoS_2 nanoflowers with expanded interlayers as high-performance anodes for sodium-ion batteries *Angew. Chem. Int. Edit* **53** 12794–8
[16] Hong X, Liu J Q, Zheng B, Huang X, Zhang X, Tan C L, Chen J Z, Fan Z X and Zhang H 2014 A universal method for preparation of noble metal nanoparticle-decorated transition metal dichalcogenide nanobelts *Adv. Mater.* **26** 6250–4
[17] Voiry D, Salehi M, Silva R, Fujita T, Chen M, Asefa T, Shenoy V B, Eda G and Chhowalla M 2013 Conducting $MoS_{(2)}$ nanosheets as catalysts for hydrogen evolution reaction *Nano Lett.* **13** 6222–7
[18] Yin W *et al* 2014 High-throughput synthesis of single-layer MoS_2 nanosheets as a near-infrared photothermal-triggered drug delivery for effective cancer therapy *ACS Nano* **8** 6922–33
[19] Jia J, Xu F, Wang S, Jiang X, Long Z and Hou X 2014 Two-dimensional MoS_2 nanosheets as a capillary GC stationary phase for highly effective molecular screening *Analyst* **139** 3533
[20] Eda G and Maier S A 2013 Two-dimensional crystals: managing light for optoelectronics *ACS Nano* **7** 5660–5
[21] Baugher B W, Churchill H O, Yang Y and Jarillo-Herrero P 2013 Intrinsic electronic transport properties of high-quality monolayer and bilayer MoS_2 *Nano Lett.* **13** 4212–6

[22] Mak K F, Lee C, Hone J, Shan J and Heinz T F 2010 Atomically thin MoS_2: a new direct-gap semiconductor *Phys. Rev. Lett.* **105** 136805

[23] Li H, Yu K, Lei X, Guo B, Fu H and Zhu Z 2015 Hydrothermal synthesis of novel $MoS_2/BiVO_4$ hetero-nanoflowers with enhanced photocatalytic activity and a mechanism investigation *J. Phys. Chem.* C **119** 22681–9

[24] Li Q, Zhang N, Yang Y, Wang G and Ng D H 2014 High efficiency photocatalysis for pollutant degradation with MoS_2/C_3N_4 heterostructures *Langmuir* **30** 8965–72

[25] Hu K H, Hu X G, Xu Y F and Sun J D 2010 Synthesis of nano-MoS_2/TiO_2 composite and its catalytic degradation effect on methyl orange *J. Mater. Sci.* **45** 2640–8

[26] Min Y, He G, Xu Q and Chen Y 2014 Dual-functional MoS_2 sheet-modified CdS branch-like heterostructures with enhanced photostability and photocatalytic activity *J. Mater. Chem.* A **2** 2578

[27] Singh N, Jabbour G and Schwingenschlögl U 2012 Optical and photocatalytic properties of two-dimensional MoS_2 *Euro. Phys. J.* B **85**

[28] Hu K H, Hu X G, Xu Y F and Pan X Z 2010 The effect of morphology and size on the photocatalytic properties of MoS2 *React. Kinetics, Mech. Catal.* **100** 153–63

[29] Qin S, Lei W, Liu D and Chen Y 2014 *In-situ* and tunable nitrogen-doping of MoS_2 nanosheets *Sci. Rep.* **4** 7582

[30] Tongay S, Varnoosfaderani S S, Appleton B R, Wu J and Hebard A F 2012 Magnetic properties of MoS_2: existence of ferromagnetism *Appl. Phys. Lett.* **101** 123105

[31] Inumaru K, Baba K and Yamanaka S 2006 Preparation of superconducting molybdenum nitride MoNx ($0.5 \leqslant x \leqslant 1$) films with controlled composition *Physica* B **383** 84–5

[32] Zhou W, Hou D, Sang Y, Yao S, Zhou J, Li G, Li L, Liu H and Chen S 2014 MoO_2 nanobelts@ nitrogen self-doped MoS_2 nanosheets as effective electrocatalysts for hydrogen evolution reaction *J. Mater. Chem.* A **2** 11358–64

[33] Shuxian Z, Hall W K, Ertl G and Knözinger H 1986 X-ray photoemission study of oxygen and nitric oxide adsorption on MoS_2 *J. Catal.* **100** 167–75

[34] Jin Q Q, Zhu X H, Xing X Y and Ren T Z 2012 Adsorptive removal of cationic dyes from aqueous solutions using graphite oxide *Adsorpt. Sci. Technol.* **30** 437–47

[35] Yao Y, Cai Y, Lu F, Qin J, Wei F, Xu C and Wang S 2014 Magnetic $ZnFe_2O_4$–C_3N_4 hybrid for photocatalytic degradation of aqueous organic pollutants by visible light *Ind. Eng. Chem. Res.* **53** 17294–302

[36] Wang X J, Yang W Y, Li F T, Xue Y B, Liu R H and Hao Y J 2013 *In situ* microwave-assisted synthesis of porous N-TiO_2/g-C_3N_4 heterojunctions with enhanced visible-light photocatalytic properties *Ind. Eng. Chem. Res.* **52** 17140–50

[37] Zhou X, Lu J, Jiang J, Li X, Lu M, Yuan G, Wang Z, Zheng M and Seo H J 2014 Simple fabrication of N-doped mesoporous TiO2 nanorods with the enhanced visible light photocatalytic activity *Nanoscale Res. Lett.* **9** 34

[38] Asahi R, Morikawa T, Ohwaki T, Aoki K and Taga Y 2001 Visible-light photocatalysis in nitrogen-doped titanium oxides *Science* **293** 269–71

[39] Hu Z Y, Xu L B and Chen J F 2013 Ordered arrays of N-doped mesoporous titania spheres with high visible light photocatalytic activity *Mater. Lett.* **106** 421–4

[40] Xiang Q, Yu J and Jaroniec M 2011 Preparation and enhanced visible-light photocatalytic H_2-production activity of graphene/C3N4Composites *J. Phys. Chem.* C **115** 7355–63

[41] Sun L, Qi Y, Jia C J, Jin Z and Fan W 2014 Enhanced visible-light photocatalytic activity of g-C_3N_4/Zn_2GeO_4 heterojunctions with effective interfaces based on band match *Nanoscale* **6** 2649–59

[42] Chen Z, Sun P, Fan B, Zhang Z and Fang X 2014 *In situ* template-free ion-exchange process to prepare visible-light-active g-C3N4/NiS hybrid photocatalysts with enhanced hydrogen evolution activity *J. Phys. Chem.* C **118** 7801–7

[43] Dai K, Lu L, Liu Q, Zhu G, Wei X, Bai J, Xuan L and Wang H 2014 Sonication assisted preparation of graphene oxide/graphitic-$C_{(3)}N_{(4)}$ nanosheet hybrid with reinforced photocurrent for photocatalyst applications *Dalton Trans.* **43** 6295–9

[44] He Y, Cai J, Li T, Wu Y, Lin H, Zhao L and Luo M 2013 Efficient degradation of RhB over $GdVO_4/g$-C_3N_4 composites under visible-light irradiation *Chem. Eng. J.* **215-216** 721–30

[45] Kong M, Li Y Z, Chen X, Tian T T, Fang P F, Zheng F and Zhao X J 2011 Tuning the relative concentration ratio of bulk defects to surface defects in TiO_2 nanocrystals leads to high photocatalytic efficiency *J. Am. Chem. Soc.* **133** 16414–7

[46] Katsumata H, Sakai T, Suzuki T and Kaneco S 2014 Highly efficient photocatalytic activity of g-C_3N_4/Ag_3PO_4 hybrid photocatalysts through Z-scheme photocatalytic mechanism under visible light *Ind. Eng. Chem. Res.* **53** 8018–25

[47] Zhang S W, Li J X, Zeng M Y, Zhao G X, Xu J Z, Hu W P and Wang X K 2013 *In situ* synthesis of water-soluble magnetic graphitic carbon nitride photocatalyst and its synergistic catalytic performance *ACS Appl. Mater. Interf.* **5** 12735–43

[48] Jiang D L, Zhu J J, Chen M and Xie J M 2014 Highly efficient heterojunction photocatalyst based on nanoporous g-C_3N_4 sheets modified by Ag_3PO_4 nanoparticles: synthesis and enhanced photocatalytic activity *J. Colloid. Interf. Sci.* **417** 115–20

[49] Lee T, Jeon E K and Kim B-S 2014 Mussel-inspired nitrogen-doped graphene nanosheet supported manganese oxide nanowires as highly efficient electrocatalysts for oxygen reduction reaction *J. Mater. Chem.* A **2** 6167

[50] He Z, Zhu Z, Li J, Zhou J and Wei N 2011 Characterization and activity of mesoporous titanium dioxide beads with high surface areas and controllable pore sizes *J. Hazard. Mater.* **190** 133–9

[51] Song F, Su H, Han J, Lau W M, Moon W-J and Zhang D 2012 Bioinspired hierarchical tin oxide scaffolds for enhanced gas sensing properties *J. Phys. Chem.* C **116** 10274–81

[52] Liu Y, Li Y, Li W, Han S and Liu C 2012 Photoelectrochemical properties and photocatalytic activity of nitrogen-doped nanoporous WO_3 photoelectrodes under visible light *Appl. Surf. Sci.* **258** 5038–45

[53] Xuan S H, Jiang W Q, Gong X L, Hu Y and Chen Z Y 2009 Magnetically separable Fe_3O_4/TiO_2 hollow spheres: fabrication and photocatalytic activity *J. Phys. Chem.* C **113** 553–8

[54] Xie T, Xu L, Liu C, Yang J and Wang M 2014 Magnetic composite BiOCl-$SrFe_{12}O_{19}$: a novel p-n type heterojunction with enhanced photocatalytic activity *Dalton Trans.* **43** 2211–20